2023 IEEE/RSJ International Conference on Intelligent Robots and Systems (IROS)
October 1-5, 2023. Detroit, USA

Vine Robot Localization Via Collision

Eugenio Frias-Miranda[1], Alankriti Srivastava[1], Sicheng Wang[1], and Laura H. Blumenschein[1]

***Abstract*— Localization of robots is a complex task that is often hindered by the sensors these systems use. Due to the majority of field robots being rigid, most of these sensing modalities have the same common faults, such as performance being hindered when their camera vision is obscured. In addition, rigid systems lack flexibility when traversing multiple environments: especially when traversing uneven and unpredictable ground. Soft robots, which can adaptably interact with the environment, could serve as a solution to both problems. One specific soft robot, the Vine Robot, has exhibited excellent performance while moving through constrained, unpredictable environments. This makes the Vine Robot an ideal candidate for a novel method of sensing and localizing in environments, obstacle collision localization. We use our understanding of the nature of Vine Robot motion to be able to predict the tip position of the robot at every instant based on sensor feedback. Through the single obstacle experiments, it was found that our algorithm can provide a precise picture of the tip position of the robot in differing environments. Further, in a multi obstacle demonstration, less than 5% max error relative to the full robot length was observed on the path prediction. Our study helps lay the foundation for a new method for Vine Robot localization using contact as a new sensing modality.**

I. Introduction

For a robot to efficiently carry out a desired task, it must know where it is, which requires both an environment map and the robot's position. Simultaneous Localization and Mapping (SLAM) has been a major focus area of the robotics community for decades [1]. In general, the position of the robot is found by acquiring scene information and constructing a map by using the positioning [2]. A range of techniques for localization have been developed such as Extended Kalman Filter SLAM (EKF-SLAM) [3], Particle Filter [4], and many more [5], [6], [7], [8]. Sensing modalities for rigid robots with SLAM [9] primarily include non-contact sensing: ultrasonic [10], Laser range Finders [11], [12], Stereo Vision [13] and RGB-D depth sensors [14], [15]. Localization of soft robots is more difficult due to their compliance and complex reactions to external stimuli. However, this compliance also allows for exteroception (ability to feel external stimuli) through proprioception [16]. To be easily integrable with soft robots, sensors measuring shape change, i.e. local strain, should meet a few basic requirements [16] For example, they must endure interaction with the outside world and must avoid interfering with the robot's compliance. Due to the difficulty in integrating sensors with soft robots, one approach is to use rigid sensors like accelerometers which do not measure strain directly, but rather infer it from the known kinematics [17], [18].

[1]School of Mechanical Engineering, Purdue University, West Lafayette, IN 47907, USA
Email: {efrias, wang5239, lhblumen}@purdue.edu

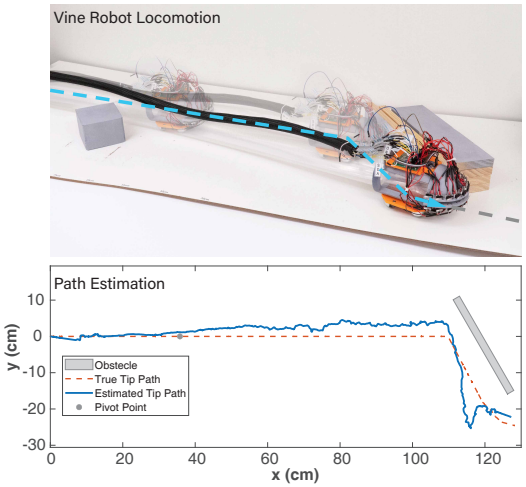

Fig. 1. Top: Vine Robot (body material: LDPE, diameter: 7 cm, max robot length: 2.4 m) interacting with a wall at 150° obstacle angle and 65cm pivot point distance. Bottom: estimated path of the tip of the robot is obtained using the proposed localization method.

Unlike rigid robots, soft robots can safely interact with their environments, opening up contact based sensing. Soft robots are made of compliant materials [19], which allows contact with the environment to shape its locomotion [20]. Snake robots have used obstacle collision to propel themselves forward [21], [22]. The question becomes, how can we leverage these responses for localization and mapping?

Vine Robots, also known as soft-growing robots, serve as a potential testbed for localizing by using the environment. Vine Robots possess a deformable structure, are pneumatically driven, and extend from the tip via pressurization [23]. Vine Robots can be passively steered by environmental interaction [20], actively steered using series pneumatic actuated muscles (sPAM) [24], or change their response to the actuation with a shape-locking mechanism [25]. Vine Robots have been applied to the fields of medicine [26], archaeology [27], and space exploration [28]. Like many soft robots, localizing Vine Robots is challenging. Cap designs to be mounted on the tip of the Vine Robot have been designed, [27], [29] and some work has looked at the kinematics of Vine Robots in contact with the environment [30], [31] or leveraging environment contact for navigation [20], [32], [33]. In this work, we build on this sensing and modeling to localize in unknown environments (Figure 1).

In this paper, we first introduce the localization method using knowledge of the Vine Robot kinematics (Section II) and designed multi-model sensing (Section III). Using this localization model, we analyze the tip position prediction (Section IV). Lastly, in Section V, we demonstrate the

2023 IEEE/RSJ International Conference on Intelligent Robots and Systems (IROS) | 978-1-6654-9190-7/23/$31.00 ©2023 IEEE | DOI: 10.1109/IROS55552.2023.10342238

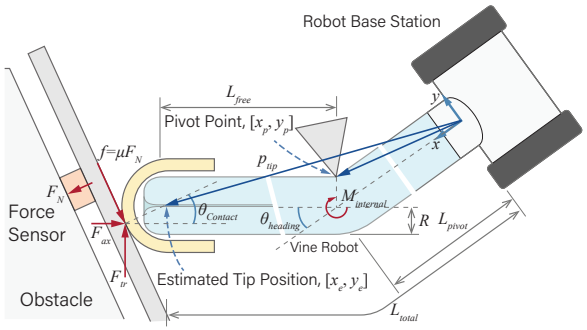

Fig. 2. Free body diagram of collision with sensorized obstacle, showing variable geometry used in the analysis. The turning of the robot at the pivot is exaggerated to illustrate the interaction with the obstacle.

localization over three obstacles.

II. Localization of a Vine Robot

A. Buckling Behavior of a Vine Robot

For a Vine Robot with only tip extension, turning occurs passively due to contact with obstacles in the environment [20], [31]. Contact with an obstacle can exist anywhere along its body. Contact at the tip induces both axial (F_{ax}, opposite to the direction of growth), and transverse (F_{tr}, perpendicular to the direction of growth) loads, resulting in potential axial and transverse buckling respectively. Axial buckling results in unpredictable behaviors, while transverse buckling creates predictable pivoting at a previous contact point. For most initial contact angles (i.e. angles 5 degrees or more away from perpendicular), previous work has shown that we should expect transverse buckling to occur [31]. Thus, to understand the configuration of a Vine Robot, the key information is the location of the turnings (the *pivot point*) induced from transverse buckling and the tip position.

Figure 2 shows the forces acting on the robot during transverse buckling, the contact angle $\theta_{contact}$, and heading angle $\theta_{heading}$. The maximum contact angle $\theta_{contact}^{\max}$ that causes transverse buckling, from Haggerty et al. [31], is:

$$\theta_{contact}^{\max} = \frac{\pi}{2} - \tan^{-1}\left(\frac{R+\mu L_{free}}{L_{free}-\mu R}\right) \tag{1}$$

where R is the radius of the Vine Robot, L_{free} is the unsupported length from the pivot point to the tip of the robot and μ is the coefficient of friction between the boundary of the Vine Robot and the surface of collision. For a given contact geometry (L_{free}, R) and friction coefficient, when $\theta_{contact} \leq \theta_{contact}^{\max}$, the transverse force component induces a moment equal to the restorative internal moment, $M_{internal}$, at the last pivot point of the robot, based on the geometry and internal pressure, P, calculated as [34] :

$$M_{internal} = F_{tr} L_{free} = \pi P R^3. \tag{2}$$

Notably, the moment depends only on the dimensions and pressure of the inflated body. Thus, with the known robot geometry and a measurement of F_{tr}, the distance between the tip and the nearest pivot point, L_{free}, can be estimated:

$$L_{free} = \frac{\pi P R^3}{F_{tr}}. \tag{3}$$

For ease of calculation, we will treat the robot as a line with zero width, so the length of the full robot (L_{total}) and distance to pivot (L_{free}), are taken from the midpoint of the robot width to the center of the end cap arc (Figure 2).

B. Localization through Collision and Buckling

While moving, Vine Robots alternate between two states: (1) a free growth state and (2) an obstacle collision state. In an unknown environment, it is possible to know a robot is in a free growth state through different sensing regimes: (1) no force at the tip ($F_{tr} = 0$), (2) no change in heading angle ($\theta_{heading} = \theta_{Prev}$, where θ_{Prev} is the last known $\theta_{heading}$ in free growth), and (3) no contact at the tip. These conditions are sufficient and necessary criteria for free growth. Using L_{free}, the $\theta_{heading}$, and the known position of the pivot $[x_P, y_P]$, the estimated tip of the robot $[x_e, y_e]$ can be calculated as:

$$\begin{aligned} x_e &= L_{free} \sin\theta_{heading} + x_P \\ y_e &= L_{free} \cos\theta_{heading} + y_P. \end{aligned} \tag{4}$$

If all three of the free growth conditions are false, a Vine Robot is in its obstacle contact state. As noted, the pivot position of a robot changes as the robot comes into contact with a new obstacle along its body and rotates around it. A change in the pivot point can be detected when the change in the L_{free} of the robot is not the same as the change in the L_{total} of the robot ($\Delta L_{free} \neq \Delta L_{total}$). The new pivot position is:

$$x_P = x_{P_{prev}} + (L_{total} - L_{free} - L_{P_{prev}}) \sin\theta_{prev} \tag{5}$$

$$y_P = y_{P_{prev}} + (L_{total} - L_{free} - L_{P_{prev}}) \cos\theta_{prev} \tag{6}$$

where $L_{P_{prev}}$ it the distance to the last known pivot point. The routine for calculating the tip position of the robot is summarized in Algorithm 1.

III. Design of Experimental Setup

A. Single Obstacle Setup

The base station's mechanical, electrical, and pneumatic components enable control of the Vine Robot's motion [27]. The robot base is a pressure vessel composed of a large acrylic cylinder with two end-caps, which stores the undeployed robot body. The base contains a 3081 Pololu Encoder, which calculates L_{total}, pressure regulators (QB3, Proportion Air, McCordsville, IN, USA), and control circuitry. An Arduino Mega 2560 and a motor driver (2A Dual Motor Controller DRI0002) control a DC motor and the pressure regulator. A switch next to the Vine Robot (body material: Low-Density Polyethylene (LDPE), diameter: 7 cm, max robot length: 2.4 m) indicates the start of an experiment.

B. Contact Sensing Cap Design

For the Single Obstacle Experiments, a contact sensing cap was designed to obtain the $\theta_{heading}$ and $\theta_{contact}$ (Figure 3). The end cap follows the movement of the Vine Robot tip, and it has a hemispherical shape for tangential collisions. Four caster wheels provide free movement. An orientation sensor (Adafruit BNO055) obtains the Vine Robot's $\theta_{heading}$, and 19 limit switches, equally spaced, measure the $\theta_{contact}$. The

Algorithm 1 Tip-position Estimation, `PathRecon()`

Input: $L_{free}^{1...N}$, $L_{total}^{1...N}$, $\theta_h^{1...N}$, $isContact^{1...N}$;
Output: $p_{tip} = \{[x_e^1 ... x_e^N], [y_e^1 ... y_e^N]\}$.

▷ Abbreviating $\theta_{heading}$ as θ_h. All inputs are $1 \times N$ array.

$p_{P_{prev}} \leftarrow [0,0]$
$L_{P_{prev}} \leftarrow 0$
$\mathbf{v}_{prev} \leftarrow [\sin(\theta_h^1) \;\; \cos(\theta_h^1)]^T$
while $i \leq N$ **do**
  if $isContact^i$ **then**
    $p_{tip}^i \leftarrow p_{P_{prev}} + (L_{total}^i - L_{free}^i - L_{P_{prev}})\mathbf{v}_{prev} + ...$
    $L_{free}^i [\sin(\theta_h^i) \;\; \cos(\theta_h^i)]^T$
    if not $isContact^{i+1}$, $i \leq N-1$ **then**
      $p_{P_{prev}} \leftarrow p_{tip}^i$
      $L_{P_{prev}} \leftarrow L_{total}^i$
    end if
  else
    $p_{tip}^i \leftarrow p_{P_{prev}} + (L_{total}^i - L_{P_{prev}}) ...$
    $[\sin(\theta_h^i) \;\; \cos(\theta_h^i)]^T$
    $\mathbf{v}_{prev} \leftarrow [\sin(\theta_h^i) \;\; \cos(\theta_h^i)]^T$
  end if
  $i++$
end while

switches were placed to maximize contact points for a more accurate $\theta_{contact}$ measurement. A communication and power tether connects the robot cap to the base station's electronics.

C. Pivot Point and Obstacle Placement Design

The experiment consists of the Vine Robot, the end cap, a pivot point block, and an adjustable obstacle. The adjustable pivot and obstacle allow for variable pivot point location and obstacle angle. Due to the thickness of the robot cap, the adjustable pivot is placed by hand after the robot tip grows past; markings keep placement consistent. The pivot point location, measured from the center of the obstacle's front panel, ranges from 35 to 75cm in 10cm increments. Given a maximum desired obstacle angle of 170 degrees, we need an inverse slenderness ratio, R/L_{free}, of 0.08 or lower to prevent axial buckling [31]. For $R = 3.5$ cm, L_{free} of the robot should be above 43.75 cm. The obstacle contained a force transducer (ATI Mini40) to measure F_{tr} and could be rotated to an angle ($\theta_{obstacle}$ ranging from 130° to 170° in increments of 10°). The force transducer was positioned in the obstacle due to constraints with the cap and to allow a higher quality sensor (ATI Mini40). While a single pivot point is used in the experiment, the algorithm is not limited to estimating single pivot changes or single pivots on obstacles, as will be shown in Section V.

D. Data Processing Method

Figure 4 gives the general architecture of the program for obtaining the tip position p_{tip} of the robot. First, the binary output of the contact switch array is converted to the contact angle $\theta_{contact}$ by averaging the resultant angles and the encoder readings are used to calculate the length of

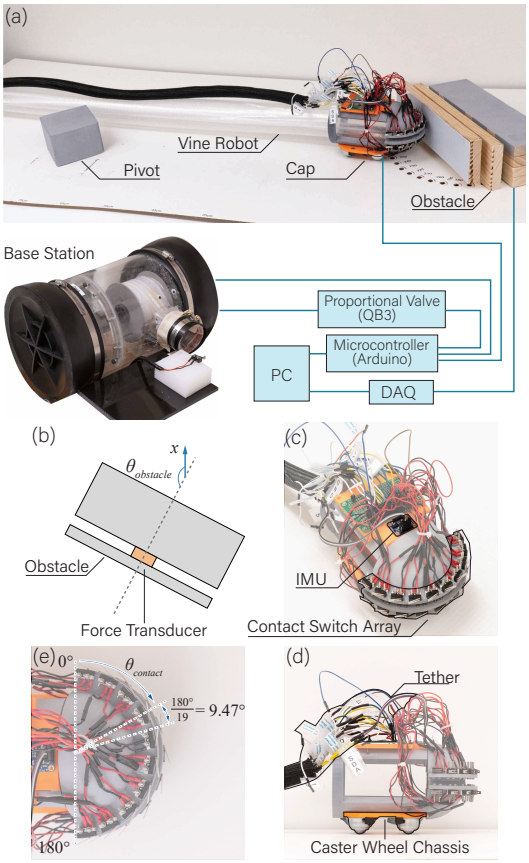

Fig. 3. (a): the components of the experiment setup. (b): a top-view diagram of the sensorized obstacle, showing the force transducer (orange) and the definition of the obstacle angle, $\theta_{obstacle}$. (c), (d): oblique and side views of robot end cap with key components labeled. (e): a close-up view of the contact switch array and the definition of the contact angle $\theta_{contact}$.

the robot, L_{total}. The routine also outputs a flag $isContact$ equal to 1 if any of the contact switches are triggered. The transverse force F_{tr} is recovered from measurement by:

$$F_{tr} = F_N \sin(\frac{\pi}{2} - \theta_{contact}), \tag{7}$$

where F_N is the normal force detected by the force transducer. L_{free} is then estimated with Equation 3 for every data point with $isContact = 1$. To reduce measurement noise, a moving average filter with a window span of 5 data is applied to the measured values of F_N and the pressure sensor, P. Additionally, an estimator is applied to recover the position of the pivot point, i.e., $L_{pivot} = L_{total} - L_{free}$. In this paper, we assume all obstacles to be polygons, so any change in pivot position would be discrete events and L_{pivot} is a piecewise constant in time. Given this assumption, a simple Kalman-based discrete estimator [35] is constructed as:

$$\begin{aligned} \hat{\mathbf{x}}_{i+1} &= \mathbf{A}\mathbf{x}_i + \mathbf{L}_i(\mathbf{z}_i - \mathbf{C}\hat{\mathbf{x}}_i) \\ \mathbf{L}_i &= \mathbf{A}\mathbf{P}_i\mathbf{C}^T(\mathbf{R}_{\mathbf{w}i} + \mathbf{C}\mathbf{P}_i\mathbf{C}^T)^{-1} \\ \mathbf{P}_{i+1} &= (\mathbf{A} - \mathbf{L_i}\mathbf{C})\mathbf{P}_i(\mathbf{A} - \mathbf{L}_i\mathbf{C})^T + \mathbf{R}_{\mathbf{v}i} + \mathbf{L}_i\mathbf{R}_{\mathbf{w}i}\mathbf{L}_i^T \end{aligned} \tag{8}$$

where $\mathbf{x} = [L_{pivot} \;\; \dot{L}_{pivot}]^T$ are the states describing the pivot position along the robot and its rate of change, and $\hat{\mathbf{x}}$ is its estimated value. $\dot{L}_{pivot}$ is obtained by finite difference of

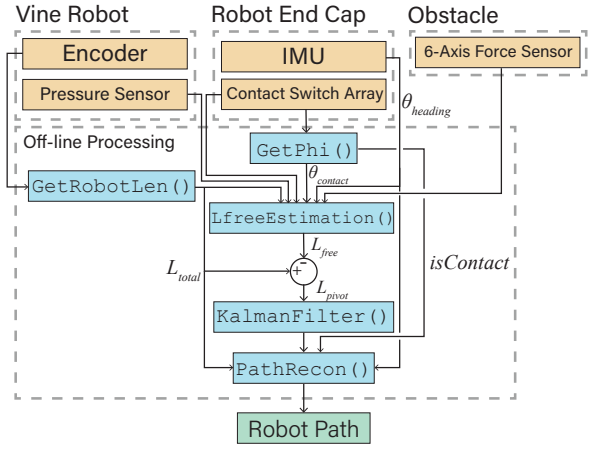

Fig. 4. Flowchart depicting the logic to obtain actual Vine Robot tip position. The hierarchy of major components, both hardware and software, are shown along with key variables.

L_{pivot}. The matrices in Equation 8 are defined as:

$$\mathbf{A} = \begin{bmatrix} 1 & \Delta t \\ 0 & \varepsilon \end{bmatrix}; \ \mathbf{C} = \mathbf{I}_{2\times 2};$$
$$\mathbf{R}_{\mathbf{w}i} = \begin{bmatrix} \sigma(L_{pivot,1\ldots i}) & 0 \\ 0 & \sigma(\dot{L}_{pivot,1\ldots i}) \end{bmatrix}, \ \mathbf{R}_{\mathbf{v}} = \begin{bmatrix} k_1 & 0 \\ 0 & k_2 \end{bmatrix}; \tag{9}$$

Since we assume L_{pivot} to be constant, $0 < \varepsilon \leq 1$ is a constant chosen to attenuate any velocity in the estimated state $\hat{\mathbf{x}}$. $\mathbf{R}_{\mathbf{v}}$ and $\mathbf{R}_{\mathbf{w}}$ are the covariance matrices of the process noise and measurement noise respectively. In this application, we interpret $\mathbf{R}_{\mathbf{v}}$ and $\mathbf{R}_{\mathbf{w}}$ as a relative measure of our confidence in the estimation based on the assumption and measured values. In Equation 9, $\mathbf{R}_{\mathbf{w}}$ is composed of the variance of L_{pivot} and $\dot{L}_{pivot}$, from the ten data points preceding the i^{th} measurement. The factors k_1 and k_2 in $\mathbf{R}_{\mathbf{v}}$ are factors chosen to reflect the confidence in the constant-value assumption relative to the measurement. The values of ε, k_1, and k_2 need to be selected heuristically and are assigned the values of 0.1, 0.1, and 1 in our implementation.

Finally, the tip path of the robot is reconstructed with *PathRecon*() routine as described in Algorithm 1. Due to the design of the estimator, L_{pivot} is used in place of L_{free}, but this does not alter the algorithm as L_{free} can be readily obtained from L_{pivot} and L_{total}. The method described in this section is implemented as an offline program for this work. Since no global information is needed in each step, it is possible to restructure the implementation for real-time localization. This would be investigated in future work.

IV. Single Obstacle Interaction Experiments

A. Direct Sensor Measurements

We measured the $\theta_{contact}$, $\theta_{heading}$, and F_{tr} plotted against L_{total} for each experiment, an example of which is shown in Figure 5. Some drift was observed in $\theta_{heading}$ over the robot's movement, so separate calibration tests were used to estimate and subtract the average drift per distance traveled from $\theta_{heading}$. Repetitions of the same angle and pivot appear to be consistent with one another. Increasing $\theta_{obstacle}$ leads

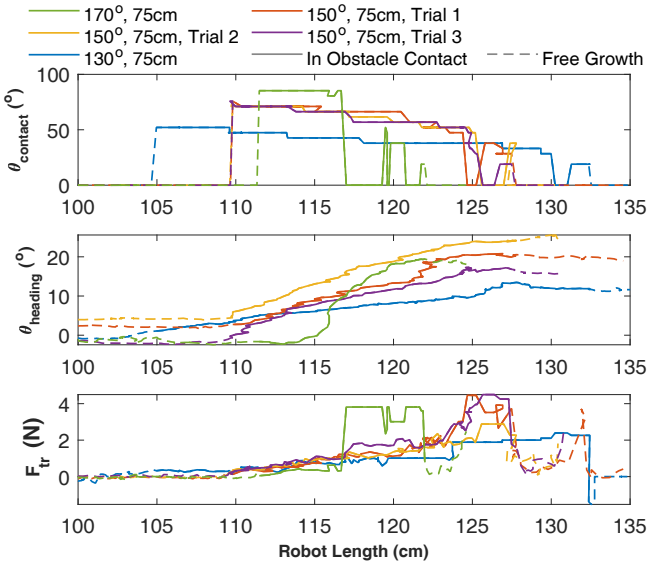

Fig. 5. From top down: unprocessed data obtained from end cap ($\theta_{contact}$, $\theta_{heading}$) and sensorized obstacle (F_{tr}) are plotted against robot length. The data while in contact with the obstacle are shown in solid lines and otherwise in dashed lines. 3 trials of the median obstacle angle ($\theta_{obstacle} = 150°$) are shown with one trial of the minimum and maximum angle ($\theta_{obstacle} = 130°$, 170°) considered in the experiments. All trials are conducted with a 75cm pivot-to-obstacle distance.

to a larger $\theta_{contact}$ and a larger change in $\theta_{heading}$. Finally, F_{tr} shows a similar range across all tests due to the L_{pivot} being the same but the gentlest angle (130°) has a lower F_{tr}, while the steepest wall angle (130°) has a lower F_{tr}. The fluctuation in force measurement is significant due to the effect of friction and intermittent contact between the robot and the obstacle. A similar effect is observed for $\theta_{contact}$, where a reading that drops to 0 suggests the end cap is not in contact with the obstacle, even if it remains in contact later. To mitigate the effect, the data processing algorithm holds the previous reading during the loss of contact.

B. Pivot Point Location

The pivot location along the robot (L_{pivot}) computed according to Section III-D is shown in Figure 6. In Figure 6(a) the average estimated pivot position $\bar{L}_{pivot}$ and its standard deviation σ_{pivot} are plotted for each combination of testing setup geometry; Figure 6(b) shows the errors in the pivot estimate. Each value of $\bar{L}_{pivot}$ and its associated σ_{pivot} is obtained over all estimations throughout the robot's contact with the obstacle. The result shows a systematic underestimation of the pivot position and significant measurement uncertainty, with larger errors for pivots placed farther from the base and obstacles at a smaller $\theta_{obstacle}$. We concluded that the error results from two major sources: first, the pressure at the tip of the robot may be lower than the sensor-reported value measured closer to the air supply, resulting in a higher estimated tip-to-pivot distance L_{free} and hence smaller L_{pivot}; Second, the intermittent loss of contact between the obstacle and the robot results in zero readings.

To recover a more reliable and consistent value of L_{pivot}, an estimator was applied to the results (Section III-D). In Figure 6(c) the distribution of estimated L_{free} for $\theta_{obstacle} =$

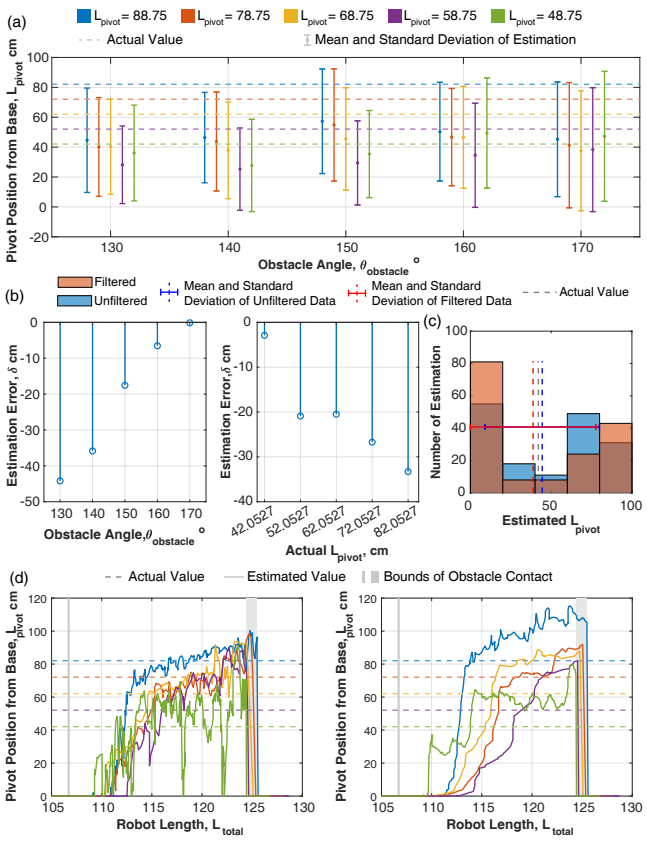

Fig. 6. (a): estimated pivot position along the robot. Color indicates the estimation made under a set pivot position. (b): estimated value error. (c): distribution of the estimated L_{free} before and after the estimator is applied. The mean and standard deviation of both and the ground-truth value are also shown. The values are obtained from a set of data collected with $\theta_{obstacle} = 140°$ and pivot-obstacle distance of 45cm. (d): the unfiltered (*left*) and filtered (*right*) L_{free} for $\theta_{obstacle} = 150°$ at various base-to-pivot distances. The robot exists the obstacle at a range of L_{total} as the robot takes a different geometry with varying placement of the pivot.

140°, pivot-obstacle distance = 45cm, is shown along with $\bar{L}_{pivot}$, σ_{pivot} and the ground truth value of L_{free}. The unfiltered data shows a dual-modal distribution with estimation concentrated both near the true value and near zero. As the Kalman filter assumes the process noise and measurement noise to be zero-mean, the filter was unable to correct the mean estimation for the result that is biased towards zero, but to reduce σ_{pivot} to some extent. Figure 6(d) further shows the evolution of L_{free} throughout contact with the obstacle.

The raw estimation *(left)* shows a ramp-up behavior from the pivot location at the base to a final value near the actual location of the pivot, with noise from the contact force measurement. The initial estimations may be incorrect as the transverse buckling assumption, as described in Equation 1, is broken due to contact geometry and friction. While attenuating noise, the application of the filter *(right)* has limited efficacy for recovering the true pivot position. Due to the assumed dynamics of the filter, which aims to reduce instantaneous change in the filtered data, the recovery from initial zero-valued measurement is slower than the raw data.

The errors observed in the experiment may be corrected with improved hardware design and better filtering. Ongoing work is also investigating a method to estimate L_{pivot}

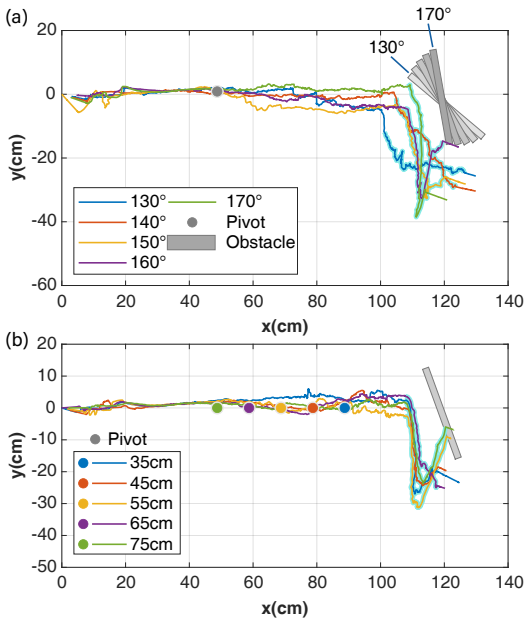

Fig. 7. (a): the tip position for 5 trials with varying $\theta_{obstacle}$ between 130°and 170°using the proposed localization method. The pivot is 75cm from the obstacle. (b): the tip position for 5 trials of varying pivot-to-obstacle positions between 35cm and 75cm. The obstacle is positioned at 160°. Tip position is plotted as the center of the cap, $R = 6$cm.

geometrically from the time series of $\theta_{contact}$, $\theta_{heading}$ and L_{total}, which potentially improves accuracy and precision by utilizing measurements of greater confidence.

C. Actual Tip Position

The tip position localization results of the single obstacle experiments are shown in Figure 7. Varying obstacle angle results in a clear difference in the path angle and for the $L_{pivot} \in [35, 75]$, 160° trials the tip position shows growth about various pivot point locations and consistent growth along the 160° obstacle. Fluctuations in the estimated tip position may be linked to noise found in the force sensor as well as orientation sensor drift. It is also important to note that the tip position is the center of the end cap, meaning we do not expect the tip position to reach the obstacle.

We next found the amount of error throughout the robot's length. The error is the distance between the actual and ideal tip position of the robot (Figure 8a-b). The tip position error tends to increase when the robot reaches the obstacle, which is likely linked to the pivot estimation. The root mean square error (RMSE) for each trial (Figure 8c-d) shows that as the pivot point gets closer to the obstacle RMSE increases, and a steeper angle also appears to increase RMSE, though only slightly. It is noted that due to the geometry of the experimental setup, the mean error observed in the path estimation is generally smaller than that of the pivot point estimation in Figure 6.

V. Multi Obstacle Demonstration

After analyzing the algorithm's behavior with a single obstacle interaction, we demonstrate the performance of the localization algorithm in a more complex environment of

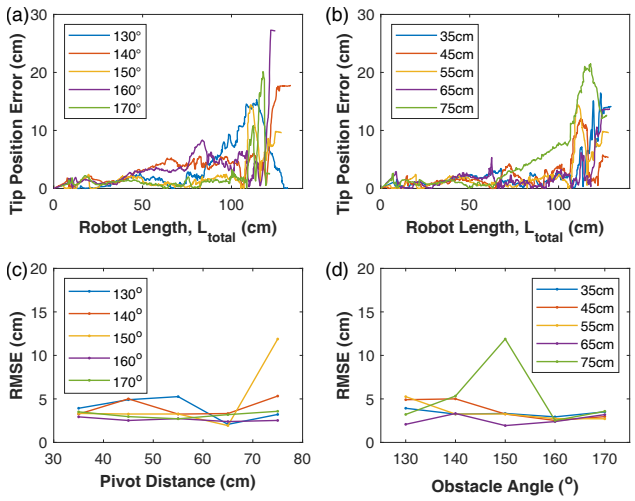

Fig. 8. (a): Error in tip position at 55cm using various $\theta_{obstacle}$. (b): Error in tip position at 150° at various L_{pivot}. (c): RMSE with obstacle placed at 55cm from pivot point using various $\theta_{obstacle}$. (d): RMSE with obstacle placed at 150° at various L_{pivot}.

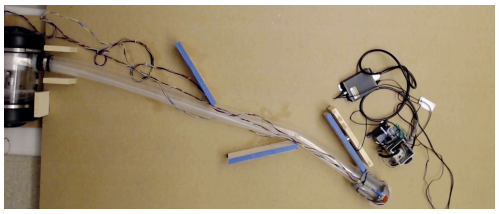

Fig. 9. Robot shape after 3 collisions

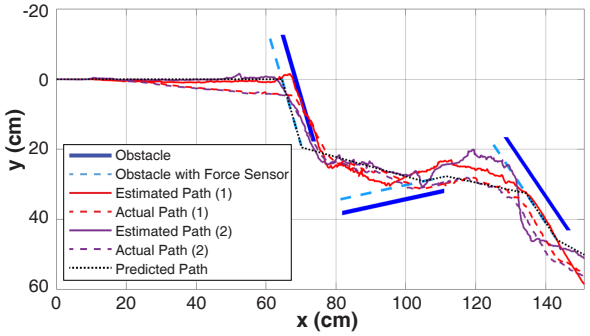

Fig. 10. Calculated tip coordinate location. The solid lines show the tip location calculated using sensors. The dashed lines show the tip position calculated from an overhead camera. The dotted line is the predicted tip position for the robot. (1) refers to dataset 1 and (2) refers to dataset 2. This figure shows only the robot's tip position, not its overall shape.

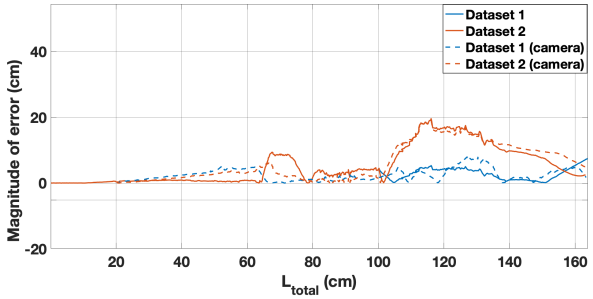

Fig. 11. Magnitude of error with respect to total length for interaction with obstacle 3. The solid lines show the error with respect to the predicted path of the camera. The dashed line shows the error with respect to the actual path of the robot recorded by the camera

three obstacles. The obstacles in the experimental setup are placed such that the $\theta_{contact}$ the robot makes on collision and the L_{free} always satisfy the condition of transverse buckling. For this experiment, $\theta_{contact}$ is calculated using an overhead camera due to errors in the measurement from the cap. Figure 9 shows the robot shape after it has finished traversing through the created environment. To create the dataset for the localization algorithm, the force sensor is mounted on one obstacle at a time. The 3 datasets created for each collision are then combined to create one dataset to localize the robot in the entire environment at every instant. As seen in Figure 10, the robot starts growing with the base of the robot as the pivot point. The initial $\theta_{heading}$ is 0 and the robot continues moving in this direction until it collides with the first obstacle. No change in the $\theta_{heading}$ indicates that there is no collision with the environment or change in pivot point.

The collision of the robot with an obstacle is indicated by a non-zero force value and a change in the $\theta_{heading}$. From the overhead camera, the $\theta_{contact}$ with the first obstacle starts at 30° to 60° after which the robot leaves this obstacle. The L_{free} is calculated using F_{tr} (Equation 3) and is approximately the same as the length calculated from the encoder values. Thus it is known that there is no change in the pivot point. The $[x_e, y_e]$ are calculated using Equation 4, with $[x_P, y_P]$ as $(0,0)$ and L_{free} as the length computed from the encoder. After leaving the first obstacle, the robot continues to grow in the direction it has left the obstacle in, and the last contact point is recorded for the pivot position, $[x_{P_{prev}}, y_{P_{prev}}]$, and length to pivot, $L_{P_{prev}}$. Collision with the second obstacle is detected similar to the first. The $\theta_{contact}$ for this interaction ranges from approximately 50° to 75°. From Figure 9, we see that this collision causes the robot to now pivot about the first obstacle. The end coordinates of the robot are now calculated using Equation (5) and (6). The calculations of the changed pivot point lead to further inaccuracies in the calculations of the end coordinates. As the robot continues to grow, it has its final collision with the third obstacle. The $\theta_{contact}$ for this collision ranges from 50° to 72°. It can be seen from Figure 9 that this collision also causes a change in pivot point to the second obstacle.

To examine the performance of the localization algorithm, we calculate the path error of the sensed tip coordinates relative to the ideal predicted path, with points aligned by total robot length and error calculated by the L2 norm; the error with respect to the actual path recorded by the overhead camera is also calculated (Figure 11). The RMSE for the first and second datasets is 3.22cm and 7.65cm, respectively. The maximum error, 20cm, represents 5% error relative to the full length of the robot. It can be seen that the error increases sharply at two points where the pivot point changes.

VI. Conclusion and Future Work

We presented a method of localization via obstacle collisions. Our setup used a sensorized end cap at the tip of the Vine Robot alongside a sensorized environment. In the pivot identification experiments, we robustly demonstrated that the

algorithm is capable of detecting pivot point changes and localizing the Vine Robot tip. Through the multi obstacle demonstration, a less than 5% error in tip position was observed using an overhead camera for validation, suggesting the robot error is on par with other soft robot results.

Future work will explore adding more obstacles to the pivot identification experiment, accommodating force sensing on the tip of the Vine Robot, and creating a non-force-based approach for tip localization with geometry as a center point. While the main objective of this work was to localize the Vine Robot tip, this work may serve as a baseline to map the environment as well. The Vine Robot can be deployed at multiple different angles from the start point to travel through a different path and map the obstacles along that path.

VII. Acknowledgements

The authors thank the ME Shop for support and Jennifer Lai for aid during the experiments and cap design.

References

[1] C. Cadena, L. Carlone, H. Carrillo, Y. Latif, D. Scaramuzza, J. Neira, I. Reid, and J. J. Leonard, "Past, present, and future of simultaneous localization and mapping: Toward the robust-perception age," *IEEE Transactions on robotics*, vol. 32, no. 6, pp. 1309–1332, 2016.

[2] K. Inoue, K. Wada, and Y. Ito, "Effective application of paro: Seal type robots for disabled people in according to ideas of occupational therapists," in *Computers Helping People with Special Needs: 11th International Conference, ICCHP*. Springer, 2008, pp. 1321–1324.

[3] R. Smith, M. Self, and P. Cheeseman, "Estimating uncertain spatial relationships in robotics," *Autonomous robot vehicles*, pp. 167–193, 1990.

[4] M. Montemerlo, S. Thrun, D. Koller, and B. Wegbreit, "Fastslam: A factored solution to the simultaneous localization and mapping problem," *Aaai/iaai*, vol. 593598, 2002.

[5] K. Yousif, A. Bab-Hadiashar, and R. Hoseinnezhad, "An overview to visual odometry and visual SLAM: Applications to mobile robotics," *Intelligent Industrial Systems*, vol. 1, no. 4, pp. 289–311, 2015.

[6] M. C. Koval, M. R. Dogar, N. S. Pollard, and S. S. Srinivasa, "Pose estimation for contact manipulation with manifold particle filters," in *2013 IEEE/RSJ International Conference on Intelligent Robots and Systems*. IEEE, 2013, pp. 4541–4548.

[7] I. Abraham, A. Mavrommati, and T. D. Murphey, "Data-driven measurement models for active localization in sparse environments," *arXiv preprint arXiv:1806.00112*, 2018.

[8] N. J. Kong, J. J. Payne, G. Council, and A. M. Johnson, "The salted kalman filter: Kalman filtering on hybrid dynamical systems," *Automatica*, vol. 131, p. 109752, 2021.

[9] T. Chong, X. Tang, C. Leng, M. Yogeswaran, O. Ng, and Y. Chong, "Sensor technologies and simultaneous localization and mapping (SLAM)," *Procedia Computer Science*, vol. 76, pp. 174–179, 2015.

[10] A. Burguera, Y. González, and G. Oliver, "Sonar sensor models and their application to mobile robot localization," *Sensors*, vol. 9, no. 12, pp. 10 217–10 243, 2009.

[11] A. Martinelli, V. Nguyen, N. Tomatis, and R. Siegwart, "A relative map approach to slam based on shift and rotation invariants," *Robotics and Autonomous Systems*, vol. 55, no. 1, pp. 50–61, 2007.

[12] V. Srinivasan and R. Lumia, "A pseudo-interferometric laser range finder for robot applications," *IEEE Transactions on Robotics and Automation*, vol. 5, no. 1, pp. 98–105, 1989.

[13] T. Lemaire, C. Berger, I.-K. Jung, and S. Lacroix, "Vision-based SLAM: Stereo and monocular approaches," *International Journal of Computer Vision*, vol. 74, no. 3, pp. 343–364, 2007.

[14] H. Gonzalez-Jorge, B. Riveiro, E. Vazquez-Fernandez, J. Martínez-Sánchez, and P. Arias, "Metrological evaluation of microsoft kinect and asus xtion sensors," *Measurement*, vol. 46, no. 6, pp. 1800–1806, 2013.

[15] K. Khoshelham and S. O. Elberink, "Accuracy and resolution of kinect depth data for indoor mapping applications," *Sensors*, vol. 12, no. 2, pp. 1437–1454, 2012.

[16] H. Wang, M. Totaro, and L. Beccai, "Toward perceptive soft robots: Progress and challenges," *Advanced Science*, vol. 5, no. 9, p. 1800541, 2018.

[17] A. M. Gruebele, A. C. Zerbe, M. M. Coad, A. M. Okamura, and M. R. Cutkosky, "Distributed sensor networks deployed using soft growing robots," in *IEEE International Conference on Soft Robotics (RoboSoft)*. IEEE, 2021, pp. 66–73.

[18] M. M. Coad, *Design, Modeling, and Control of Vine Robots for Exploration of Unknown Environments*. Stanford University, 2021.

[19] D. Rus and M. T. Tolley, "Design, fabrication and control of soft robots," *Nature*, vol. 521, no. 7553, pp. 467–475, 2015.

[20] J. D. Greer, L. H. Blumenschein, R. Alterovitz, E. W. Hawkes, and A. M. Okamura, "Robust navigation of a soft growing robot by exploiting contact with the environment," *The International Journal of Robotics Research*, vol. 39, no. 14, pp. 1724–1738, 2020.

[21] A. A. Transeth, R. I. Leine, C. Glocker, K. Y. Pettersen, and P. Liljebäck, "Snake robot obstacle-aided locomotion: Modeling, simulations, and experiments," *IEEE Transactions on Robotics*, vol. 24, no. 1, pp. 88–104, 2008.

[22] P. Liljeback, K. Y. Pettersen, Ø. Stavdahl, and J. T. Gravdahl, "Snake robot locomotion in environments with obstacles," *IEEE/ASME Transactions on Mechatronics*, vol. 17, no. 6, pp. 1158–1169, 2011.

[23] E. W. Hawkes, L. H. Blumenschein, J. D. Greer, and A. M. Okamura, "A soft robot that navigates its environment through growth," *Science Robotics*, vol. 2, no. 8, p. eaan3028, 2017.

[24] J. D. Greer, T. K. Morimoto, A. M. Okamura, and E. W. Hawkes, "Series pneumatic artificial muscles (spams) and application to a soft continuum robot," in *IEEE International Conference on Robotics and Automation (ICRA)*. IEEE, 2017, pp. 5503–5510.

[25] S. Wang, R. Zhang, D. A. Haggerty, N. D. Naclerio, and E. W. Hawkes, "A dexterous tip-extending robot with variable-length shape-locking," in *IEEE International Conference on Robotics and Automation (ICRA)*. IEEE, 2020, pp. 9035–9041.

[26] P. Slade, A. Gruebele, Z. Hammond, M. Raitor, A. M. Okamura, and E. W. Hawkes, "Design of a soft catheter for low-force and constrained surgery," in *IEEE/RSJ International Conference on Intelligent Robots and Systems (IROS)*. IEEE, 2017, pp. 174–180.

[27] M. M. Coad, L. H. Blumenschein, S. Cutler, J. A. R. Zepeda, N. D. Naclerio, H. El-Hussieny, U. Mehmood, J.-H. Ryu, E. W. Hawkes, and A. M. Okamura, "Vine robots," *IEEE Robotics & Automation Magazine*, vol. 27, no. 3, pp. 120–132, 2019.

[28] N. D. Naclerio, C. M. Hubicki, Y. O. Aydin, D. I. Goldman, and E. W. Hawkes, "Soft robotic burrowing device with tip-extension and granular fluidization," in *IEEE/RSJ International Conference on Intelligent Robots and Systems (IROS)*. IEEE, 2018, pp. 5918–5923.

[29] S.-G. Jeong, M. M. Coad, L. H. Blumenschein, M. Luo, U. Mehmood, J. H. Kim, A. M. Okamura, and J.-H. Ryu, "A tip mount for transporting sensors and tools using soft growing robots," in *IEEE/RSJ International Conference on Intelligent Robots and Systems (IROS)*. IEEE, 2020, pp. 8781–8788.

[30] L. H. Blumenschein, A. M. Okamura, and E. W. Hawkes, "Modeling of bioinspired apical extension in a soft robot," in *Biomimetic and Biohybrid Systems: 6th International Conference, Living Machines 2017, Stanford, CA, USA, July 26–28, 2017, Proceedings 6*. Springer, 2017, pp. 522–531.

[31] D. A. Haggerty, N. D. Naclerio, and E. W. Hawkes, "Characterizing environmental interactions for soft growing robots," in *IEEE/RSJ International Conference on Intelligent Robots and Systems (IROS)*. IEEE, 2019, pp. 3335–3342.

[32] M. Selvaggio, L. Ramirez, N. D. Naclerio, B. Siciliano, and E. W. Hawkes, "An obstacle-interaction planning method for navigation of actuated vine robots," in *IEEE International Conference on Robotics and Automation (ICRA)*. IEEE, 2020, pp. 3227–3233.

[33] F. Fuentes and L. H. Blumenschein, "Mapping unknown environments through passive deformation of soft, growing robots," in *IEEE International Conference on Intelligent Robots and Systems*. IEEE, 2023.

[34] W. Fichter, *A Theory for Inflated Thin-wall Cylindrical Beams*, ser. A Theory for Inflated Thin-wall Cylindrical Beams. National Aeronautics and Space Administration, Langley Research Center, 1966, no. v. 3466.

[35] K. Åström and R. Murray, *Feedback Systems: An Introduction for Scientists and Engineers, Second Edition*. Princeton University Press, 2021. [Online]. Available: https://books.google.com/books?id=l50DEAAAQBAJ